J. Fluid Mech. (2004), *vol.* 516, *pp.* 211–238.
DOI: 10.1017/S0022112004000680 Printed in the United Kingdom

Unstable density stratification of miscible fluids in a vertical Hele-Shaw cell: influence of variable viscosity on the linear stability

By N. GOYAL AND E. MEIBURG†

Department of Mechanical and Environmental Engineering, University of California, Santa Barbara, CA 93106, USA

(Received 21 April 2003 and in revised form 18 May 2004)

The influence of viscosity variations on the density-driven instability of two miscible fluids in a vertical Hele-Shaw cell is investigated by means of a linear stability analysis. Dispersion relations are presented for different Rayleigh numbers, viscosity ratios and interfacial thickness parameters of the base concentration profile. The analysis employs the three-dimensional Stokes equations, and the results are compared with those obtained from the variable density and viscosity Hele-Shaw equations. While the growth rate does not depend on which of the two fluids is the more viscous, the maxima of the eigenfunctions are always seen to shift towards the less viscous fluid. For every parameter combination, the dominant instability mode is found to be three-dimensional. With increasing viscosity ratio, the instability is uniformly damped. For a fixed viscosity ratio, both the growth rate and the most unstable wavenumber increase monotonically with the Rayleigh number, until they asymptotically reach a plateau.

Surprising findings are obtained regarding the effects of varying the interface thickness. At higher viscosity ratios the largest growth rates and unstable wavenumbers are observed for intermediate thicknesses. This demonstrates that for variable viscosities thicker interfaces can be more unstable than their thinner counterparts, in contrast to the constant viscosity case. The reason behind this behaviour can be traced to the influence of the gap width on the vertical extent of the perturbation eigenfunctions. For thick interfaces, the eigenfunction can reside almost entirely within the interfacial region. In that way, the perturbation maximum is free to shift towards the less viscous fluid, i.e. into a locally more unstable environment. In contrast, for thin interfaces, the eigenfunction is forced to extend far into the viscous fluid, which leads to an overall stabilization. While the Hele-Shaw analysis also captures this 'optimal' growth for intermediate interface thicknesses, the growth rates differ substantially from those obtained from the full Stokes equations. Compared to the Hele-Shaw results, growth rates obtained from the modified Brinkman equation are seen to yield better quantitative agreement with the Stokes results.

1. Introduction

The analysis of density-driven instabilities between miscible fluids of constant viscosity in a vertical Hele-Shaw cell dates back at least to the classical work by

† Author to whom correspondence should be addressed: meiburg@engineering.ucsb.edu

Wooding (1960). A review of the literature on this topic is provided by Fernandez *et al.* (2002) and Graf, Meiburg & Härtel (2002). These authors employ experiments, direct numerical simulations and a linear stability analysis based on the three-dimensional Stokes equations, in order to obtain further insight. The different sets of results obtained by these approaches, which are generally in close agreement with each other, indicate the existence of a low-Rayleigh-number regime in which the dominant wavelength is inversely proportional to the Rayleigh number, and a high-Rayleigh-number regime with a dominant wavelength about five times the gap width of the Hele-Shaw cell. In particular, the linear stability analysis shows that the maximum growth rate increases uniformly with the Rayleigh number, until it asymptotically reaches a plateau. In contrast, it decreases monotonically as the interface thickness grows. Graf *et al.* (2002), furthermore, conduct a corresponding linear stability analysis based on the Hele-Shaw equations, and they observe large discrepancies between the results from this analysis and those based on the full Stokes equations. Similar discrepancies between Stokes-based results and predictions from Hele-Shaw theory are known to occur in immiscible Hele-Shaw flows as well, cf. Maxworthy (1989) and Park & Homsy (1984). Since Hele-Shaw flows are frequently employed to study viscosity-driven instabilities (Homsy 1987), it is of interest to expand the linear stability analysis of Graf *et al.* (2002) to include variable viscosity effects. This is the topic of the present investigation.

The physical problem along with the governing equations and dimensionless parameters are described in § 2. That section also presents the linearization of the equations and the formulation of the numerical eigenvalue problem. Section 3 discusses the findings for both two- and three-dimensional perturbations, and it compares the results from the Stokes-based analysis with predictions based on the Hele-Shaw equations as well as the modified Brinkman equation. Section 4 summarizes the main findings and points to future work.

2. Physical problem

2.1. *Governing equations*

We consider two miscible fluids of different density and viscosity in a vertical Hele-Shaw cell, as shown in figure 1. The heavier fluid is placed above the lighter one, thus giving rise to an unstable density stratification. We will analyse situations in which either the heavier or the lighter fluid is the more viscous one. For narrow gaps, the flow velocities will be very small, so that the fluid motion is governed by the three-dimensional Stokes equations

$$\nabla \cdot \boldsymbol{u} = 0, \tag{2.1}$$

$$\nabla p = \nabla \cdot \boldsymbol{\tau} + \rho \boldsymbol{g}, \tag{2.2}$$

$$c_t + \boldsymbol{u} \cdot \nabla c = D \nabla^2 c. \tag{2.3}$$

Here, $\boldsymbol{u}$ denotes the flow velocity, $\boldsymbol{g}$ represents the acceleration due to gravity, which is taken to point in the $-y$-direction, and c indicates the relative concentration of the heavier, upper fluid. $\boldsymbol{\tau}$ denotes the viscous stress tensor, while D represents the diffusion coefficient, which is assumed constant. The cell has a gap of width e, with z indicating the gapwise direction. The x-direction will be referred to as the spanwise direction.

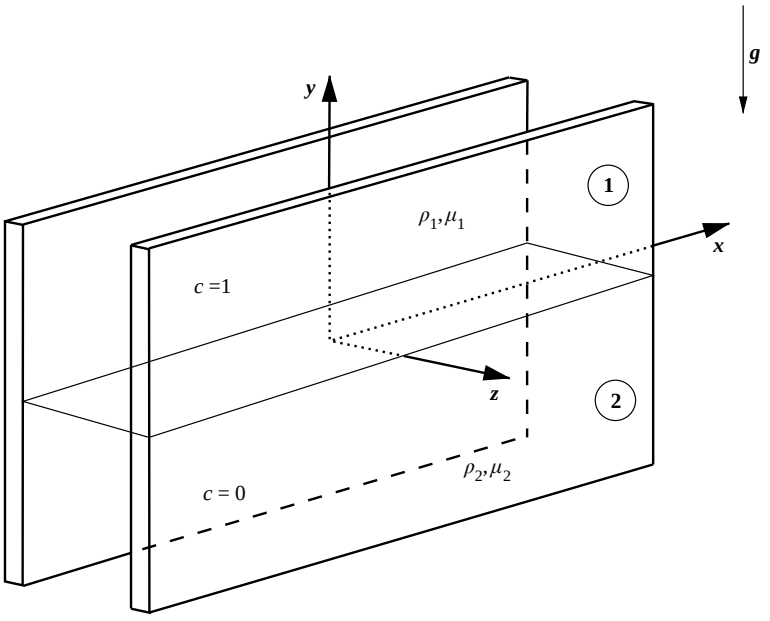

FIGURE 1. Geometry of the Hele-Shaw cell. The heavier fluid is placed above the lighter one. Either of the fluids can be the more viscous one.

In following other authors, the density ρ and the viscosity μ are assumed to be linear and exponential functions of the concentration c, respectively,

$$\rho = \rho_2 + c(\rho_1 - \rho_2), \tag{2.4}$$

$$\mu = \mu_2 \mathrm{e}^{Rc}. \tag{2.5}$$

ρ_1 and μ_1 indicate the density and viscosity of the heavier fluid, while ρ_2 and μ_2 represent the counterparts for the lighter fluid. The logarithm R of the viscosity ratio is defined as

$$R = \ln \frac{\mu_1}{\mu_2}. \tag{2.6}$$

The governing equations are rendered dimensionless by introducing a characteristic length L^*, velocity U^*, time T^*, pressure P^* and density difference G^* in the form of

$$L^* = e, \tag{2.7}$$

$$U^* = \frac{\Delta\rho g e^2}{\mu_{min}}, \tag{2.8}$$

$$T^* = \frac{\mu_{min}}{\Delta\rho g e}, \tag{2.9}$$

$$P^* = \Delta\rho g e, \tag{2.10}$$

$$G^* = \Delta\rho = \rho_1 - \rho_2. \tag{2.11}$$

Note that the non-dimensionalization is always carried out with the smaller viscosity, so that a meaningful comparison can be made between cases in which either the lighter or the heavier fluid is more viscous. Hence, when the lighter fluid is more viscous $\mu_{min} = \mu_1$, and when the heavier fluid is more viscous $\mu_{min} = \mu_2$. An alternative way towards non-dimensionalizing the governing equations is proposed by Martin, Rakotomalala & Salin (2002) for situations in which the viscosities of both fluids are

identical. These authors employ an intrinsic length scale based on the fluid properties, rather than the gap width. This approach allows them to address situations ranging from narrow gaps to unbounded fluids. However, it results in the emergence of an additional dimensionless parameter. Furthermore, it is not straightforward to extend this approach to variable viscosity fluids. For this reason, the present investigation employs the gap width as the characteristic length scale.

We thus obtain the set of dimensionless equations as

$$0 = u_x + v_y + w_z, \tag{2.12}$$

$$p_x = 2f_x u_x + f_y(u_y + v_x) + f_z(u_z + w_x) + f\nabla^2 u, \tag{2.13}$$

$$p_y = f_x(u_y + v_x) + 2f_y v_y + f_z(v_z + w_y) + f\nabla^2 v - c, \tag{2.14}$$

$$p_z = f_x(u_z + w_x) + f_y(v_z + w_y) + 2f_z w_z + f\nabla^2 w, \tag{2.15}$$

$$0 = c_t + \boldsymbol{u}\cdot\nabla c - \frac{1}{Ra}\nabla^2 c, \tag{2.16}$$

where

$$f = \mathrm{e}^{Rc}, \tag{2.17}$$

$$Ra = \frac{\Delta\rho g e^3}{D\mu_{min}}. \tag{2.18}$$

The Rayleigh number Ra indicates the relative strength of the buoyancy-induced convection and the transport by diffusion.

2.2. *Linearization*

In order to conduct the linear stability analysis, the above set of dimensionless equations is linearized around a one-dimensional quiescent base state. We assume that the perturbation growth is characterized by a time scale that is much shorter than that describing the diffusive changes of the base state. As a result of this quasi-steady state approximation (cf. Tan & Homsy 1986), we can ignore the time dependence of the base state, so that we obtain

$$u(x, y, z, t) = \bar{u}(y) + u'(x, y, z, t), \tag{2.19}$$

$$v(x, y, z, t) = \bar{v}(y) + v'(x, y, z, t), \tag{2.20}$$

$$w(x, y, z, t) = \bar{w}(y) + w'(x, y, z, t), \tag{2.21}$$

$$p(x, y, z, t) = \bar{p}(y) + p'(x, y, z, t), \tag{2.22}$$

$$c(x, y, z, t) = \bar{c}(y) + c'(x, y, z, t). \tag{2.23}$$

The base state around which the linearization is carried out is defined as follows:

$$\bar{p} = \bar{p}(y), \tag{2.24}$$

$$\bar{u} = 0, \tag{2.25}$$

$$\bar{v} = 0, \tag{2.26}$$

$$\bar{w} = 0, \tag{2.27}$$

$$\bar{c} = 0.5 + 0.5\ \mathrm{erf}\left(\frac{y}{\delta}\right), \tag{2.28}$$

where δ represents the thickness of the diffusive interfacial layer separating the two fluids. We assume wavelike perturbations of the form

$$u'(x, y, z, t) = \hat{u}(y, z)\sin(\beta x)\mathrm{e}^{\sigma t}, \tag{2.29}$$

$$v'(x, y, z, t) = \hat{v}(y, z)\cos(\beta x)\mathrm{e}^{\sigma t}, \tag{2.30}$$

$$w'(x, y, z, t) = \hat{w}(y, z)\cos(\beta x)\mathrm{e}^{\sigma t}, \tag{2.31}$$

$$p'(x, y, z, t) = \hat{p}(y, z)\cos(\beta x)\mathrm{e}^{\sigma t}, \tag{2.32}$$

$$c'(x, y, z, t) = \hat{c}(y, z)\cos(\beta x)\mathrm{e}^{\sigma t}. \tag{2.33}$$

Here, variables marked with ˆ represent the perturbation amplitudes. Upon substituting these expressions into the governing equations, the base state is subtracted out, and all terms quadratic in the disturbances are neglected. For the case in which the heavier fluid is the more viscous, i.e. $\mu_{min} = \mu_2$, we thus obtain

$$\beta\hat{u} + \hat{v}_y + \hat{w}_z = 0, \tag{2.34}$$

$$\beta\hat{p} + \mathrm{e}^{R\bar{c}}(-\beta^2 + \partial_{yy} + \partial_{zz} + R\bar{c}_y\partial_y)\hat{u} - \beta R\mathrm{e}^{R\bar{c}}\bar{c}_y\hat{v} = 0, \tag{2.35}$$

$$-\hat{p}_y + \mathrm{e}^{R\bar{c}}(-\beta^2 + \partial_{yy} + \partial_{zz} + 2R\bar{c}_y\partial_y)\hat{v} - \hat{c} = 0, \tag{2.36}$$

$$-\hat{p}_z + \mathrm{e}^{R\bar{c}}(-\beta^2 + \partial_{yy} + \partial_{zz} + R\bar{c}_y\partial_y)\hat{w} + R\mathrm{e}^{R\bar{c}}\bar{c}_y\hat{v}_z = 0, \tag{2.37}$$

$$\bar{c}_y\hat{v} + \left[\sigma - \frac{1}{Ra}(-\beta^2 + \partial_{yy} + \partial_{zz})\right]\hat{c} = 0. \tag{2.38}$$

The above system of equations represents an eigenvalue problem with the growth rate σ as the eigenvalue, and $\hat{p}$, $\hat{u}$, $\hat{v}$, $\hat{w}$ and $\hat{c}$ as the eigenfunctions. There are four parameters in the problem, namely the wavenumber β, the Rayleigh number Ra, the viscosity parameter R and the interface thickness δ. For the case of the lighter fluid being the more viscous one, $\bar{c}$ is replaced by $\bar{c} - 1$ in the exponential terms of the above equations.

2.3. *Numerical implementation*

In order to solve the above set of equations numerically, we discretize them in a domain that extends from $-l/2$ to $l/2$ in the y-direction, and from -0.5 to 0.5 in the cross-gap z-direction, as shown in figure 2. To avoid any influence of the domain size on the numerical results, its vertical extent l is allowed to vary as a function of the dimensionless parameter values. It is taken sufficiently large so that the perturbations can be assumed to vanish at the top and bottom boundaries. At the vertical walls of the cell, we assume homogeneous Dirichlet conditions for the velocities, and a vanishing normal derivative for the concentration. No boundary conditions are required for the pressure perturbation. A Chebyshev collocation method is employed in the vertical direction. This allows us to concentrate the grid points in the interfacial region, by subdividing the domain into two equal subdomains. In the cross-gap direction, we use compact finite-difference schemes of up to tenth order in the interior of the domain, and fourth order at the boundaries (Lele 1992).

Figure 3 indicates the qualitative nature of the overall grid. We thus obtain an algebraic system of the form

$$\boldsymbol{A}\,\boldsymbol{\phi} = \sigma\,\boldsymbol{B}\,\boldsymbol{\phi}. \tag{2.39}$$

The eigenvalue σ represents the growth rate of the perturbations, while the eigenvector $\boldsymbol{\phi}$ reflects the shape of the perturbations. As usual, a positive (negative) eigenvalue indicates unstable (stable) behaviour. $\boldsymbol{A}$ and $\boldsymbol{B}$ denote the coefficient matrices. In the calculations to be discussed below, the maximum domain length in the y-direction

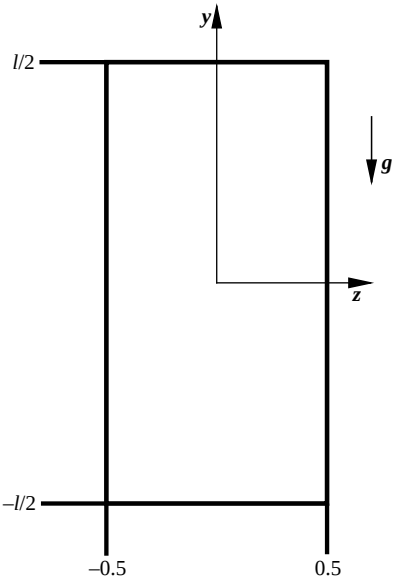

FIGURE 2. Coordinate system of the computational domain.

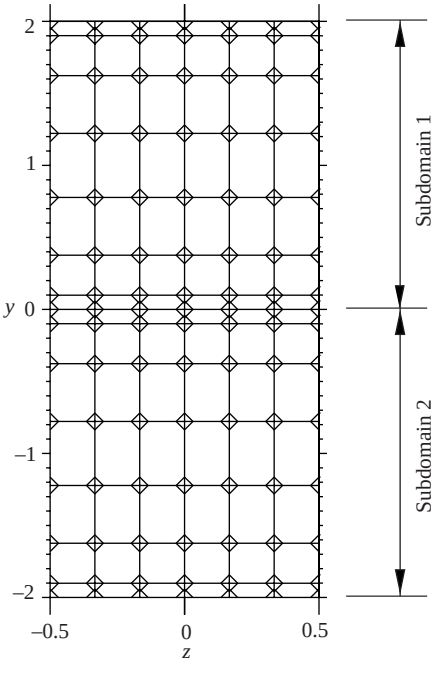

FIGURE 3. Mesh point distribution in the computational domain. A Chebyshev grid is employed in the y-direction, and compact finite differences in the z-direction.

is 140, discretized by 175 grid points. In the cross-gap direction, 25 points proved to be sufficient. Since we solve for 5 variables at each grid point, the matrix $\boldsymbol{A}$ is of the size $5\,ny\,nz \times 5\,ny\,nz$, where ny and nz are the number of grid-points in the y- and z-directions, respectively. Hence, for the largest grid, the matrix is of size

$21\,875 \times 21\,875$. The structure of the matrices is as follows

$$\begin{pmatrix} \mathbf{0} & \beta\boldsymbol{I} & \partial_y & \partial_z & \mathbf{0} \\ \beta\boldsymbol{I} & \boldsymbol{M}_1 & \boldsymbol{M}_2 & \mathbf{0} & \mathbf{0} \\ -\partial_y & \mathbf{0} & \boldsymbol{M}_3 & \mathbf{0} & -\boldsymbol{I} \\ -\partial_z & \mathbf{0} & \boldsymbol{M}_4 & \boldsymbol{M}_1 & \mathbf{0} \\ \mathbf{0} & \mathbf{0} & -\bar{\boldsymbol{c}}_y & \mathbf{0} & \boldsymbol{M}_5 \end{pmatrix} \begin{pmatrix} \hat{p} \\ \hat{u} \\ \hat{v} \\ \hat{w} \\ \hat{c} \end{pmatrix} = \sigma \begin{pmatrix} \mathbf{0} & \mathbf{0} & \mathbf{0} & \mathbf{0} & \mathbf{0} \\ \mathbf{0} & \mathbf{0} & \mathbf{0} & \mathbf{0} & \mathbf{0} \\ \mathbf{0} & \mathbf{0} & \mathbf{0} & \mathbf{0} & \mathbf{0} \\ \mathbf{0} & \mathbf{0} & \mathbf{0} & \mathbf{0} & \mathbf{0} \\ \mathbf{0} & \mathbf{0} & \mathbf{0} & \mathbf{0} & \boldsymbol{I} \end{pmatrix} \begin{pmatrix} \hat{p} \\ \hat{u} \\ \hat{v} \\ \hat{w} \\ \hat{c} \end{pmatrix},$$

with

$$\boldsymbol{M}_1 = \mathrm{e}^{R\bar{c}}[-\beta^2\boldsymbol{I} + \partial_{yy} + \partial_{zz} + R\bar{\boldsymbol{c}}_y\,\partial_y], \tag{2.40}$$

$$\boldsymbol{M}_2 = -\beta R\mathrm{e}^{R\bar{c}}\bar{\boldsymbol{c}}_y, \tag{2.41}$$

$$\boldsymbol{M}_3 = \mathrm{e}^{R\bar{c}}[-\beta^2\boldsymbol{I} + \partial_{yy} + \partial_{zz} + 2R\bar{\boldsymbol{c}}_y\,\partial_y], \tag{2.42}$$

$$\boldsymbol{M}_4 = R\mathrm{e}^{R\bar{c}}\bar{\boldsymbol{c}}_y\,\partial_z, \tag{2.43}$$

$$\boldsymbol{M}_5 = \frac{1}{Ra}(-\beta^2\boldsymbol{I} + \partial_{yy} + \partial_{zz}). \tag{2.44}$$

In order to calculate the largest eigenvalues along with the corresponding eigenvectors, we use the ARPACK package based on the Arnoldi iteration method (Sorensen 1992; Maschhoff & Sorensen 1996; Lehoucq, Sorensen & Yang 1998). Slow convergence due to an excess of zeros in the matrix $\boldsymbol{B}$ is overcome by employing the approach of Graf *et al.* (2002), which modifies the original equations slightly to

$$\nabla\cdot\boldsymbol{u} = 0, \tag{2.45}$$

$$Re\boldsymbol{u}_t + \nabla p = \nabla\cdot\boldsymbol{\tau} + \rho\boldsymbol{g}, \tag{2.46}$$

$$c_t + \boldsymbol{u}\cdot\nabla c = D\nabla^2 c. \tag{2.47}$$

The term $Re\boldsymbol{u}_t$ is added to the momentum equation to obtain additional non-zero elements on the main diagonal. Convergence tests were performed to determine the value of the Reynolds number-like parameter Re so that more rapid convergence is obtained without altering the eigenvalues and eigenfunctions by more than 0.1%. The value of $Re = 0.01$ was found to satisfy these requirements.

2.4. *Two-dimensional perturbations*

Two-dimensional perturbations confined to the (y, z)-plane are considered separately on the basis of a streamfunction vorticity-formulation. This provides an additional validation of the three-dimensional approach in the limit of small spanwise wavenumbers. The governing equations are obtained by taking the curl of the two-dimensional Stokes equations

$$\nabla^2\psi + \omega = 0, \tag{2.48}$$

$$f\nabla^2\omega + 2f_y\omega_y + 2f_z\omega_z - (f_{yy} - f_{zz})(\psi_{yy} - \psi_{zz}) - 4f_{yz}\psi_{yz} - c_z = 0, \tag{2.49}$$

$$c_t + \boldsymbol{u}\cdot\nabla c - \frac{1}{Ra}\nabla^2 c = 0. \tag{2.50}$$

Here, the vorticity ω and streamfunction ψ are defined as

$$w = \psi_y, \quad v = -\psi_z, \tag{2.51}$$

$$\omega = v_z - w_y. \tag{2.52}$$

The base state in terms of these variables is

$$\bar{\psi} = 0, \tag{2.53}$$

$$\bar{\omega} = 0, \tag{2.54}$$

while the perturbations are of the form

$$\psi' = \hat{\psi}(y,z)\mathrm{e}^{\sigma t}, \tag{2.55}$$

$$\omega' = \hat{\omega}(y,z)\mathrm{e}^{\sigma t}, \tag{2.56}$$

$$c' = \hat{c}(y,z)\mathrm{e}^{\sigma t}. \tag{2.57}$$

We again employ a Reynolds number-like term in order to accelerate convergence. After substituting the above quantities and linearizing, the eigenvalue problem in matrix form is

$$\begin{pmatrix} \boldsymbol{M}_1 & \boldsymbol{I} & \boldsymbol{0} \\ \boldsymbol{M}_2 & \boldsymbol{M}_3 & -\boldsymbol{\partial}_z \\ \boldsymbol{M}_4 & \boldsymbol{0} & \boldsymbol{M}_5 \end{pmatrix} \begin{pmatrix} \hat{\psi} \\ \hat{\omega} \\ \hat{c} \end{pmatrix} = \sigma \begin{pmatrix} \boldsymbol{0} & \boldsymbol{0} & \boldsymbol{0} \\ \boldsymbol{0} & Re\boldsymbol{I} & \boldsymbol{0} \\ \boldsymbol{0} & \boldsymbol{0} & \boldsymbol{I} \end{pmatrix} \begin{pmatrix} \hat{\psi} \\ \hat{\omega} \\ \hat{c} \end{pmatrix}, \tag{2.58}$$

with

$$\boldsymbol{M}_1 = \boldsymbol{\partial}_{yy} + \boldsymbol{\partial}_{zz}, \tag{2.59}$$

$$\boldsymbol{M}_2 = -R\mathrm{e}^{R\bar{c}}\left(\bar{\boldsymbol{c}}_{yy} + R\bar{\boldsymbol{c}}_y^2\right)(\boldsymbol{\partial}_{yy} - \boldsymbol{\partial}_{zz}), \tag{2.60}$$

$$\boldsymbol{M}_3 = \mathrm{e}^{R\bar{c}}(\boldsymbol{\partial}_{yy} + \boldsymbol{\partial}_{zz} + 2R\bar{\boldsymbol{c}}_y\ \boldsymbol{\partial}_y), \tag{2.61}$$

$$\boldsymbol{M}_4 = \bar{\boldsymbol{c}}_y\ \boldsymbol{\partial}_z, \tag{2.62}$$

$$\boldsymbol{M}_5 = \frac{1}{Ra}(\boldsymbol{\partial}_{yy} + \boldsymbol{\partial}_{zz}). \tag{2.63}$$

The boundary conditions for the streamfunction and vorticity are analogous to those in the three-dimensional problem. At the solid walls the streamfunction $\hat{\psi}$ and its wall-normal derivative $\hat{\psi}_z$ are set to zero. At the top and bottom boundaries, we assume vanishing perturbations and hence set $\hat{\psi} = \hat{\omega} = 0$.

2.5. *Analytical solution of the Stokes equations for a step profile*

In his classical work on the Rayleigh–Taylor instability, Chandrasekhar (1961) employed the Stokes equations in an unbounded domain, for a step-like base concentration profile and in the absence of diffusion. He determined the growth rates of small-amplitude perturbations as a function of the wavenumber and fluid properties. In the following, we extend this approach to obtain analytic growth rates with the effects of diffusion included. By assuming a wavelike behaviour of the perturbations in the cross-gap direction, cf. below, these results can subsequently be compared to those obtained numerically for finite-thickness base concentration profiles.

The base concentration profile is given by

$$\bar{c} = \begin{cases} 0 & \text{if } y < 0, \\ 1 & \text{if } y > 0. \end{cases} \tag{2.64}$$

The perturbations are assumed to be of the form

$$\eta'(x,y,z,t) = \hat{\eta}(y)\mathrm{e}^{\mathrm{i}(\beta x + \gamma z)}\mathrm{e}^{\sigma t}, \tag{2.65}$$

where η takes on the values of u, v, w, p and c, respectively. The subsequent elimination of pressure, concentration and the spanwise and gapwise velocities results in the following ordinary differential equation for the vertical velocity perturbation

$$\begin{aligned}(\mathrm{D}^2 - m^2)[\mathrm{e}^{R\bar{c}}(\mathrm{D}^2 - k^2)^2 + 2R(\mathrm{e}^R - 1)\delta(y)\{\mathrm{D}^3 - k^2\mathrm{D}\} \\ + R(\mathrm{e}^R - 1)\delta''(y)(\mathrm{D}^2 + k^2)]\hat{v} = -k^2 Ra\delta(y)\hat{v},\end{aligned} \tag{2.66}$$

where

$$D = \partial_y \tag{2.67}$$

$$k = \sqrt{\beta^2 + \gamma^2} \tag{2.68}$$

$$m = \sqrt{k^2 + \sigma Ra}. \tag{2.69}$$

Here, δ represents the Dirac delta function. Away from the interface ($y \neq 0$), δ vanishes and $\hat{v}$ can be expressed as

$$\hat{v}(y) = A_{\pm} e^{\mp ky} + y B_{\pm} e^{\mp ky} + C_{\pm} e^{\mp my}, \tag{2.70}$$

thereby ensuring that it decays far from the interface. Five of the six coefficients are determined by imposing the continuity of the velocity components, pressure, concentration and the normal and tangential stresses across the interface. Integration of (2.66) across the interface then yields the following equation for the growth rate σ

$$2\sigma^2(1 + e^R)\, k - \sigma = \frac{2k^2}{Ra}\left(\frac{k}{\sqrt{k^2 + \sigma Ra}} - 1\right). \tag{2.71}$$

From this expression we can determine the growth rate as a function of the wavenumber, for different Rayleigh numbers. As will be seen below, the numerical results for finite-thickness base concentration profiles suggest that two-dimensional perturbations within a finite gap display an approximately wavelike behaviour in the cross-gap direction, with the wavelength equal to the gap width, so that $\gamma = 2\pi$. For three-dimensional perturbations, on the other hand, the gap width corresponds to half a wavelength, so that $\gamma = \pi$. These values will be employed below for comparison purposes.

2.6. *Hele-Shaw equations*

Graf *et al.* (2002) compared their results obtained from the three-dimensional Stokes equations with predictions based on the Hele-Shaw equations. They found substantial discrepancies, especially for high Rayleigh numbers. Within the current investigation, we want to evaluate the influence of viscosity variations in this regard. By casting the Hele-Shaw equations for the gap-averaged quantities into the stream function, vorticity-formulation and subsequently non-dimensionalizing them with the same characteristic quantities as before, we obtain the following set of equations

$$\nabla^2 \psi = -\omega, \tag{2.72}$$

$$12(f\omega - f_x \psi_x - f_y \psi_y) = -c_x, \tag{2.73}$$

$$c_t + \boldsymbol{u} \cdot \nabla c = \frac{1}{Ra} \nabla^2 c. \tag{2.74}$$

where

$$f = e^{Rc}. \tag{2.75}$$

Here, the vorticity and streamfunction are defined as

$$u = \psi_y, \quad v = -\psi_x, \tag{2.76}$$

$$\omega = v_x - u_y. \tag{2.77}$$

These equations are linearized with regard to small perturbations that are wavelike in the spanwise direction

$$\psi'(x, y, t) = \hat{\psi}(y)\sin(\beta x)\mathrm{e}^{\sigma t}, \tag{2.78}$$

$$\omega'(x, y, t) = \hat{\omega}(y)\sin(\beta x)\mathrm{e}^{\sigma t}, \tag{2.79}$$

$$c'(x, y, t) = \hat{c}(y)\cos(\beta x)\mathrm{e}^{\sigma t}, \tag{2.80}$$

where the quantities with the $\hat{}$ symbol denote the eigenfunctions, which are now one-dimensional. The base state is the same as before. The eigenvalue problem then takes the matrix form

$$\begin{pmatrix} \boldsymbol{M}_1 & \boldsymbol{I} & \boldsymbol{0} \\ \boldsymbol{M}_2 & \boldsymbol{M}_3 & -\beta\boldsymbol{I} \\ \beta\bar{\boldsymbol{c}} & \boldsymbol{0} & \boldsymbol{M}_4 \end{pmatrix} \begin{pmatrix} \hat{\psi} \\ \hat{\omega} \\ \hat{c} \end{pmatrix} = \sigma \begin{pmatrix} \boldsymbol{0} & \boldsymbol{0} & \boldsymbol{0} \\ \boldsymbol{0} & Re\boldsymbol{I} & \boldsymbol{0} \\ \boldsymbol{0} & \boldsymbol{0} & \boldsymbol{I} \end{pmatrix} \begin{pmatrix} \hat{\psi} \\ \hat{\omega} \\ \hat{c} \end{pmatrix}, \tag{2.81}$$

with

$$\boldsymbol{M}_1 = \boldsymbol{\partial}_{yy} - \beta^2\boldsymbol{I}, \tag{2.82}$$

$$\boldsymbol{M}_2 = -12Re^{R\bar{c}}\bar{\boldsymbol{c}}_y\,\boldsymbol{\partial}_y, \tag{2.83}$$

$$\boldsymbol{M}_3 = 12e^{R\bar{c}}\boldsymbol{I}, \tag{2.84}$$

$$\boldsymbol{M}_4 = \frac{1}{Ra}(\boldsymbol{\partial}_{yy} - \beta^2\boldsymbol{I}). \tag{2.85}$$

The matrix for the Hele-Shaw problem is of size $3ny \times 3ny$, which is much smaller than for the earlier Stokes problem. We again employ an artificial Reynolds number of 0.01 in order to accelerate the rate of convergence of the ARPACK solver. At the top and bottom boundaries, we assume Dirichlet conditions for all perturbation quantities, i.e. $\hat{\psi} = \hat{\omega} = \hat{c} = 0$.

2.7. *Validation of results*

Here, we present a brief summary of various convergence and validation tests that we conducted in order to determine the accuracy of the results. Graf *et al.* (2002) had found that a vertical domain length of approximately twice the perturbation wavelength is required to resolve the eigenfunctions adequately, and to keep the error in the eigenvalues below 0.1%. We found that the domain length required for a well-converged solution does not depend on the viscosity ratio, so that we can maintain the same criterion for determining l

$$l = 2\lambda = \frac{4\pi}{\beta}. \tag{2.86}$$

For wavenumbers larger than $O(5)$, the domain length was not further reduced, as a minimum domain length is necessary in order to be able to apply the assumption that all perturbations die out at the top and bottom boundaries. For an interface thickness of $\delta = 0.1$, this minimum domain length was 4, while for a thicker interface of $\delta = 2$, it was chosen to be 7. For two-dimensional perturbations, a domain length of $l = 10$ was found to be sufficient.

Several checks were performed in order to determine the minimum number of grid points required for converged eigenvalues and well-resolved eigenvectors. We found that the number of grid points required depends on the wavenumber and the interface thickness, while it is not affected by the values of the Rayleigh number or the viscosity ratio. A thicker interface generally requires a smaller number of grid points for the same level of accuracy as compared to a thinner interface. In the cross-gap z-direction, 21 grid points were usually adequate for the three-dimensional case, and 25 points for

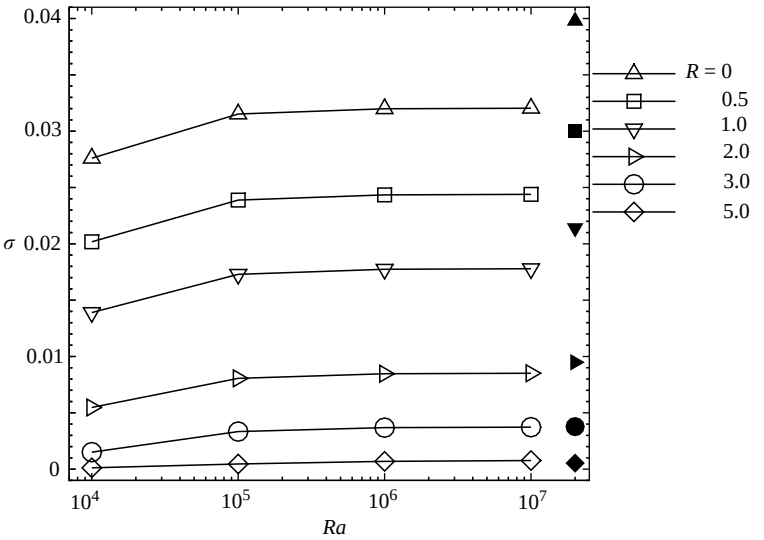

FIGURE 4. The leading eigenvalue σ for two-dimensional perturbations as a function of Ra, for $\delta = 0.1$ and different viscosity ratios. The growth rate decreases with increasing values of R. Filled symbols correspond to $\delta = 0$ and $Ra \to \infty$.

the two-dimensional problem. However, some three-dimensional calculations required as many as 25 grid points. In the y-direction, a maximum number of grid points of 175 was required for the thinnest interface of $\delta = 0.1$ and the smallest wavenumber of $\beta = 0.1$. For the two-dimensional case, the number of grid points required was 91. The above grid sizes guarantee that the growth rates are accurate to within an error margin of 0.1%.

For the constant-viscosity case of $R = 0$, our calculations reproduced the results of Graf *et al.* (2002) exactly. As we will see below, the growth rates obtained from the three-dimensional problem in the limit of $\beta \to 0$ converge to those of the corresponding two-dimensional problem. A final validation of our results is the good comparison of the results for $\delta = 0.1$ with those obtained from the analytical solution of the Stokes equations for a sharp interface between the two fluids. In some of the plots in the following results section, we plot the growth rates corresponding to this step function concentration profile to illustrate this agreement. In a similar fashion, the corresponding dispersion relation (Manickam & Homsy 1995) for the Hele-Shaw equations validates our numerical results for the Hele-Shaw equations.

3. Results

3.1. *Two-dimensional perturbations*

We begin by discussing the growth of two-dimensional perturbations. Figure 4 displays the leading eigenvalue as a function of the Rayleigh number Ra, for different values of the viscosity ratio R. The growth rate is seen to increase with Ra, until it asymptotically reaches a plateau for Rayleigh numbers greater than 10^5. This behaviour is in line with our expectations, as the driving force behind the instability grows with Ra. An increase in the logarithm of the viscosity ratio R, on the other hand, dampens the growth of the instability, owing to the higher average viscosity of the two-fluid system.

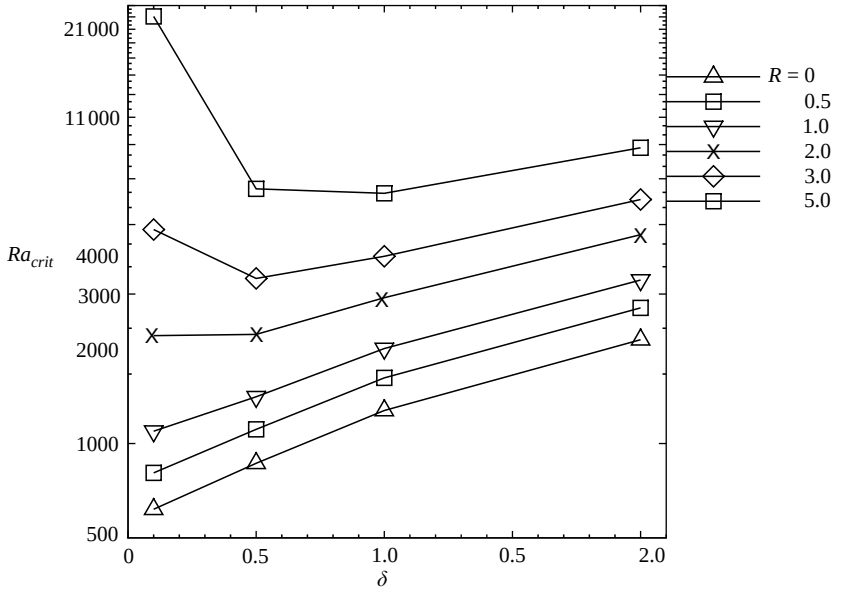

FIGURE 5. The critical Rayleigh number Ra_{crit} for two-dimensional perturbations as a function of the interface thickness, for various viscosity ratios. At small R, Ra_{crit} increases monotonically with δ, while at higher R, a minimum exists for an intermediate interface thickness.

In the limit $Ra \to \infty$, (2.71) reduces to

$$\sigma = \frac{1}{2k(1 + e^R)}, \tag{3.1}$$

which gives us this plateau value of the growth rates. These are shown by filled symbols, for each viscosity ratio, in figure 4. The growth rates for a sharp interface are higher than those for $\delta = 0.1$ for small viscosity ratios, while the reverse is true at higher viscosity ratios. The critical Rayleigh number for the system to go unstable is shown in figure 5 for various interface thicknesses and viscosity ratios. For small values of R, Ra_{crit} increases monotonically with δ, indicating that thicker interfaces are more stable. However, for R values larger than 2 we find that Ra_{crit} has a minimum at an intermediate δ value. Below this minimum, increasing the interface thickness destabilizes the system. This observation will be discussed in more detail below, in the context of three-dimensional perturbations.

Our calculations show that the growth rates do not depend on the sign of R, i.e. they are identical independently of whether the heavier or the lighter fluid is the more viscous. This result follows directly from the form of the governing equations, as will be shown below for the more general case of three-dimensional perturbations. As a consequence, we will limit our discussion to positive values of the viscosity ratio only, i.e. to cases in which the upper heavier fluid is the more viscous one. It should be noted, however, that the shape of the eigenfunctions depends on R, as shown in figure 6. While for the constant-viscosity, case, the eigenfunctions were seen to be symmetric with respect to $z = 0$ (Graf *et al.* 2002), we see a shift in the $-y$-direction for $R = 1$, and in the $+y$-direction for $R = -1$. This indicates that the maximum of the perturbations is located primarily in the less viscous fluid.

Figure 7 shows the concentration eigenfunctions for different viscosity ratios. It is evident that for larger R values the perturbation maximum increasingly shifts in

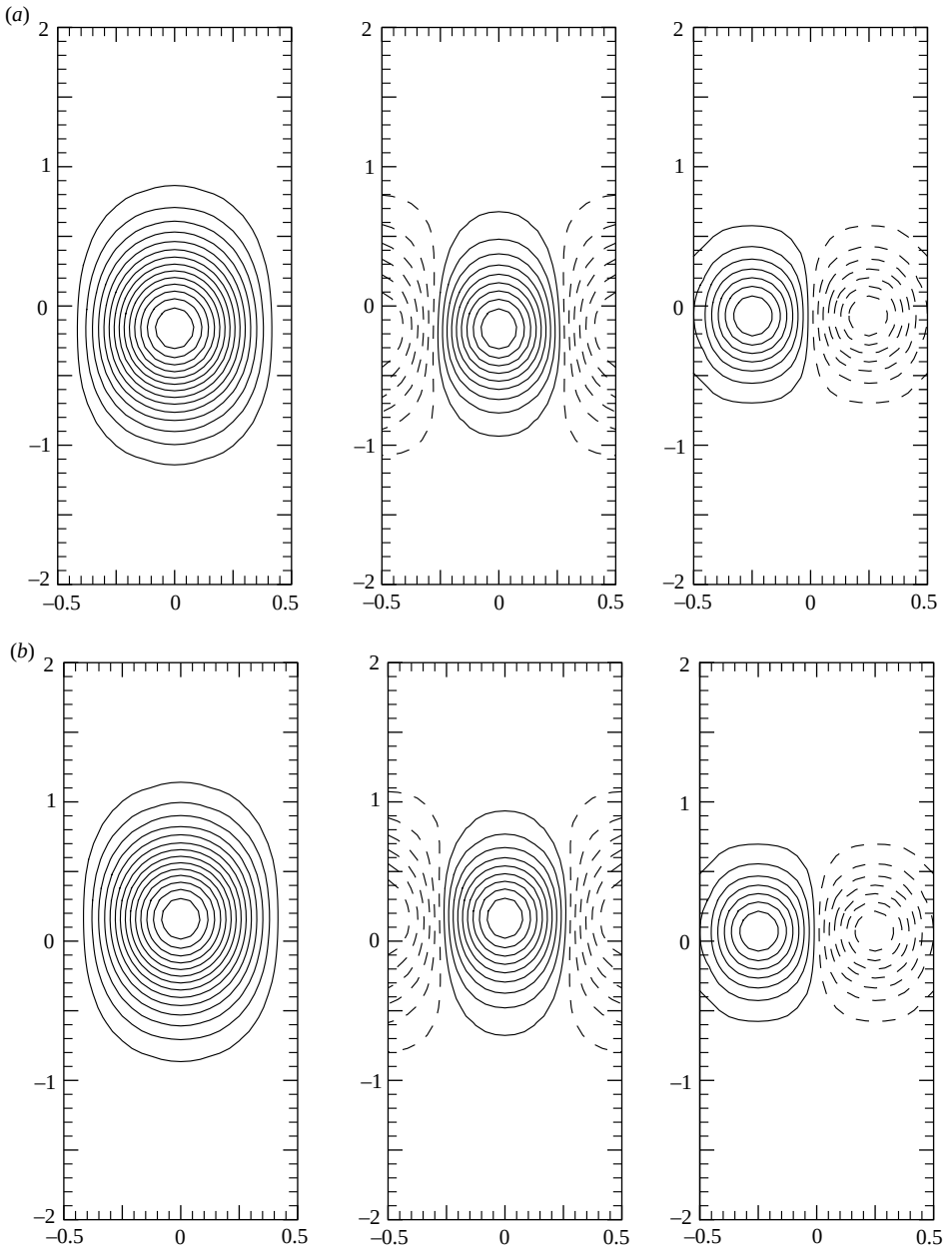

FIGURE 6. The eigenfunctions $\hat{\psi}$, $\hat{\omega}$, $\hat{c}$ for two-dimensional perturbations and $\delta = 0.5$, $Ra = 10^5$. (*a*) $R = 1$, (*b*) $R = -1$. The leading eigenvalue $\sigma = 1.08723 \times 10^{-2}$ for both cases. Solid (dashed) lines represent positive (negative) values.

the $-y$-direction, i.e. into the less viscous fluid. Figure 8 qualitatively sketches the corresponding interfacial shapes. These are obtained by adding a multiple of the concentration eigenfunction to the base concentration profile, and then plotting the $c = 0.5$ contour. It is evident that the symmetry of the emerging fingers is broken as R increases, with the more viscous downward-moving finger being narrower than the upward-propagating less viscous finger.

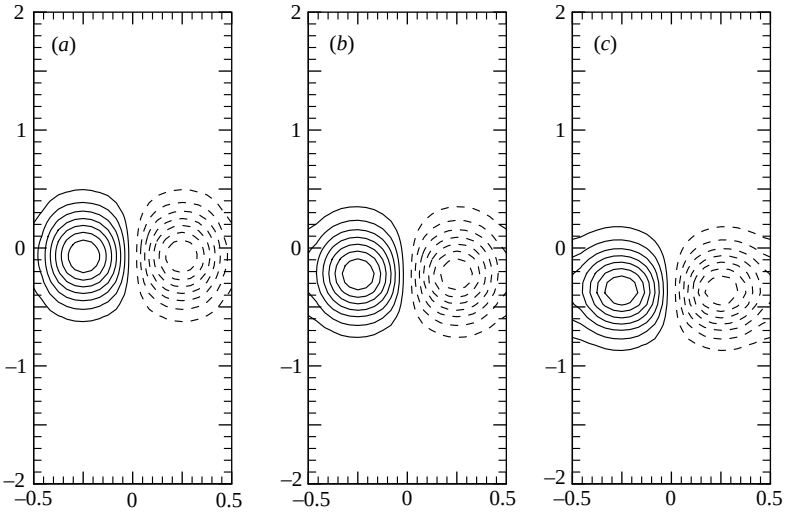

FIGURE 7. Concentration eigenfunctions of two-dimensional perturbations for $\delta = 0.5$ and $Ra = 10^5$. (*a*) $R = 1$, (*b*) $R = 3$, (*c*) $R = 5$. For growing viscosity contrasts, the perturbation maximum increasingly shifts into the less viscous fluid.

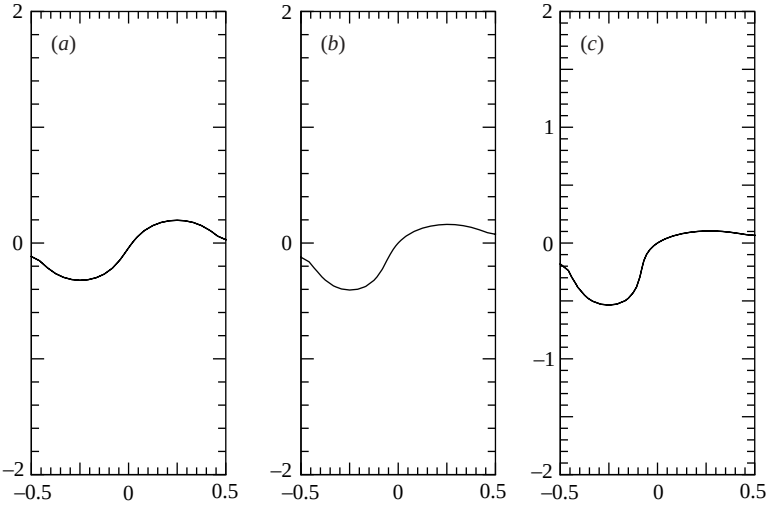

FIGURE 8. Qualitative sketch of the interfacial shapes for $\delta = 0.5$, $Ra = 10^5$ and (*a*) $R = 1$, (*b*) $R = 3$ and (*c*) $R = 5$.

For the case of constant viscosity, Graf *et al.* (2002) observed a qualitative change in the shape of the fingers as the Rayleigh number increased. For low Ra, the fingers were seen to be wider, and to propagate along the walls. On the other hand, for high Ra values, thinner fingers were found that propagate along the centre of the cell. Here, we observe a similar trend in the variable viscosity case as well. Figure 9 depicts this behaviour by showing the concentration eigenfunctions and the qualitative finger shape for the Rayleigh numbers 10^4 and 10^7, respectively. For $Ra = 10^4$, the majority of the contour lines emerge from the wall, while for $Ra = 10^7$ all contour lines are closed within the fluid. This is reflected by the different shapes of the fingers, as shown in figures 9(*c*) and 9(*d*), respectively.

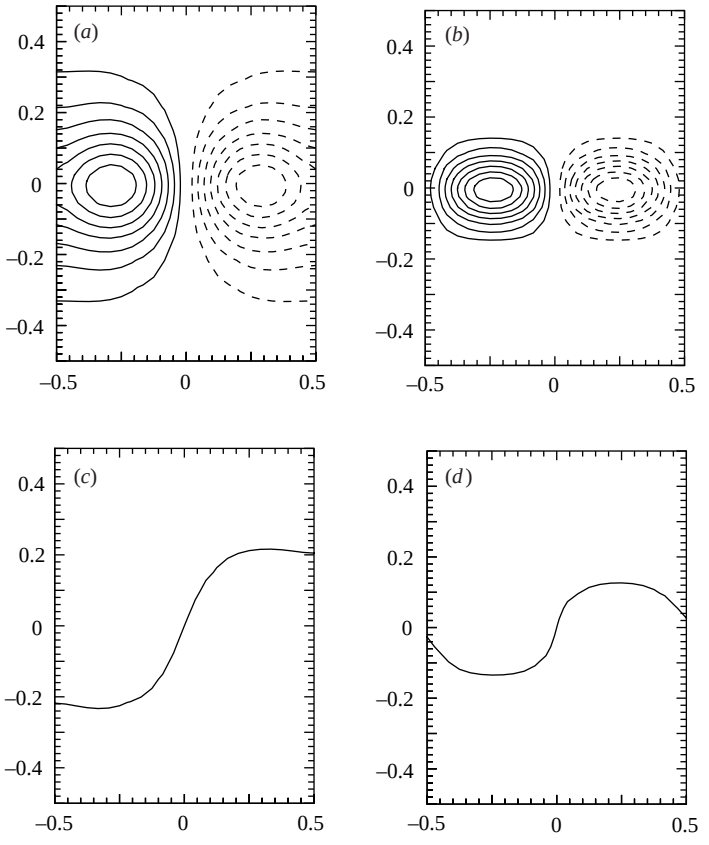

FIGURE 9. Two-dimensional perturbations for $\delta = 0.1$ and $R = 2$. Concentration eigenfunctions for (*a*) $Ra = 10^4$ and (*b*) $Ra = 10^7$, and qualitative finger shapes for (*c*) $Ra = 10^4$ and (*d*) $Ra = 10^7$.

Figure 10 shows the leading eigenvalue for $Ra = 10^7$ as a function of the interface thickness, for different values of the viscosity ratio. As mentioned above, the analytical value for $\delta = 0$ is obtained by assuming a wavelike perturbation across the gap, with a wavelength equal to the gap width, so that $k = 2\pi$. While for the constant-viscosity case the growth rate is seen to decrease uniformly with increasing δ, we find that, in the presence of substantial viscosity variations, σ can attain a maximum at an intermediate interface thickness. The figure furthermore suggests that the most unstable value of δ increases with R. This will be discussed further below, for the more general case of three-dimensional perturbations.

Figure 11 shows the growth rate as a function of the viscosity ratio for various interface thicknesses, at two different values of the Rayleigh number. It is evident that the instability of a thin interface is damped much more strongly by an increase in R, as compared to a thicker interface. This behaviour explains the observed emergence of a most unstable intermediate interface thickness at high viscosity ratios.

3.2. *Three-dimensional perturbations*

Here, we focus on perturbations that display wavelike behaviour in the spanwise direction. Figure 12 shows the leading eigenvalue as a function of the wavenumber for a constant interface thickness of $\delta = 0.1$, a Rayleigh number of $Ra = 10^5$, and for various viscosity ratios. As for the two-dimensional case, an increase in R has a

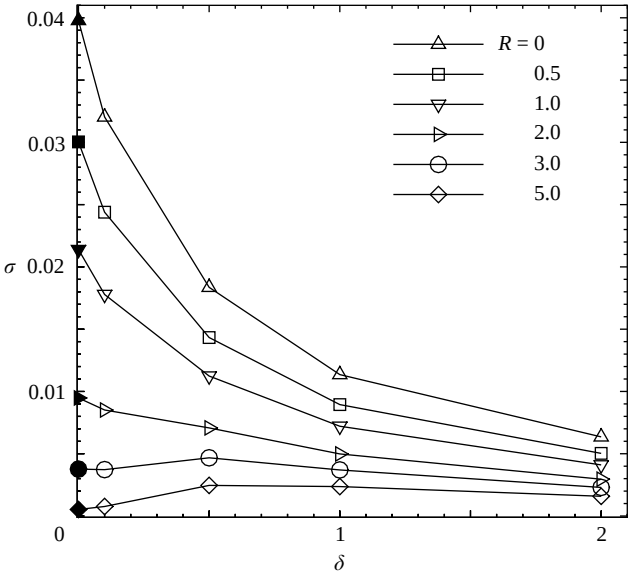

FIGURE 10. Growth rate σ as a function of the interface thickness for two-dimensional perturbations and different viscosity ratios, at $Ra = 10^7$. For $R \geqslant 3$, interfaces of intermediate thickness are most unstable. The filled symbols correspond to the analytical results for a sharp interface.

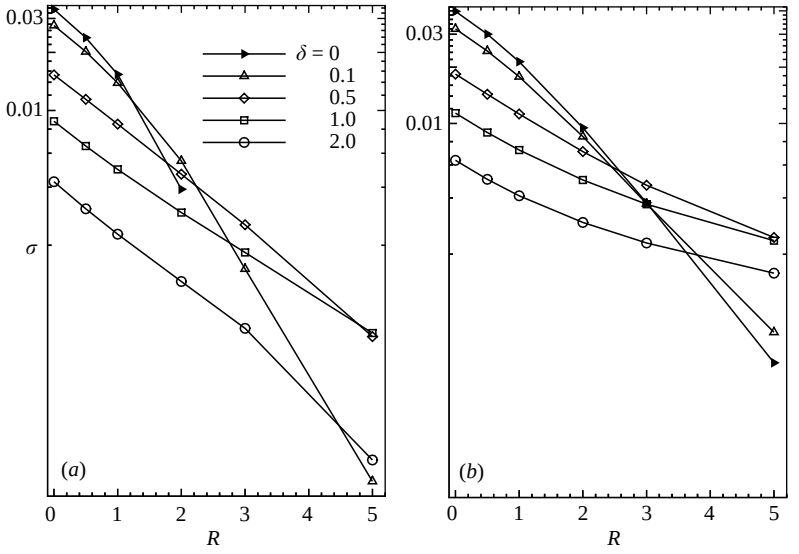

FIGURE 11. Growth rate as a function of the viscosity ratio for various interface thicknesses and (*a*) $Ra = 10^4$ and (*b*) $Ra = 10^7$. At high viscosity ratios, thicker interfaces become more unstable than thinner ones. This behaviour is somewhat more pronounced for low Rayleigh numbers than for higher Rayleigh numbers.

stabilizing effect. The results of the three-dimensional calculations are seen to converge to the two-dimensional results as $\beta \to 0$. This represents an additional validation, as the two sets of results were obtained with different computational codes. It is evident that for each set of parameters there is always a three-dimensional mode that is

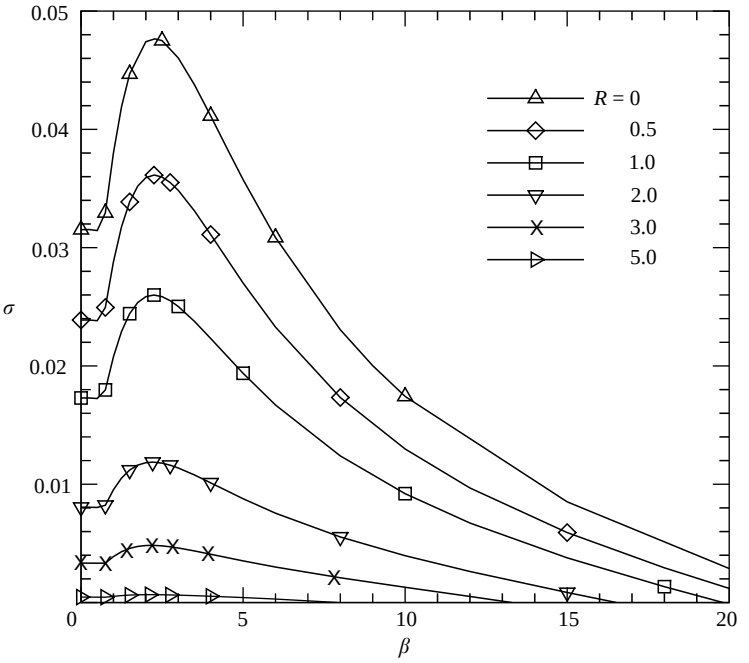

FIGURE 12. Growth rate as a function of the spanwise wavenumber for different viscosity ratios. The interface thickness is $\delta = 0.1$ and $Ra = 10^5$. Increasing viscosity ratios have a stabilizing effect.

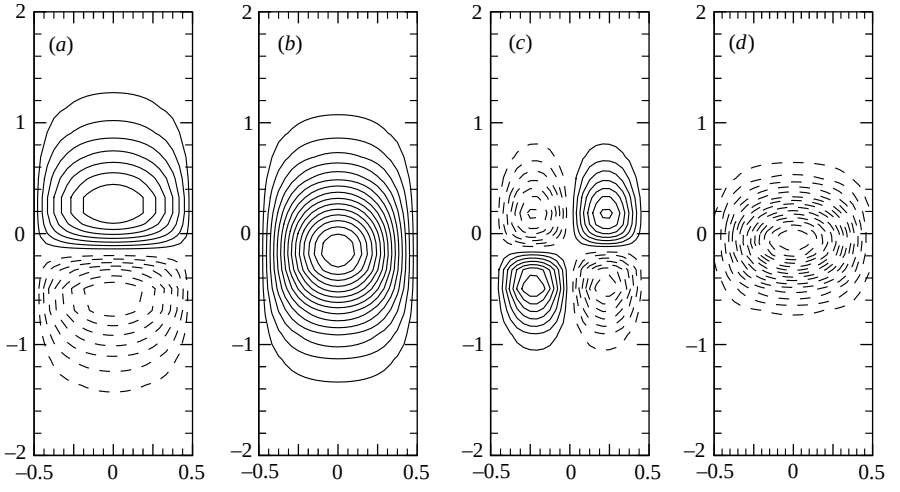

FIGURE 13. Eigenfunction contours of (*a*) $\hat{u}$, (*b*) $\hat{v}$, (*c*) $\hat{w}$ and (*d*) $\hat{c}$, $\delta = 0.5$, $Ra = 10^5$, $\beta = 4$ and $R = 1$. The eigenfunctions are shifted towards the less viscous lower fluid.

more unstable than its two-dimensional counterpart. Thus, there always exists a most dangerous and a short-wave cutoff mode. As for the two-dimensional case, the growth rate increases with the Rayleigh number, until it reaches a plateau around $Ra = 10^5$.

As mentioned above in the context of two-dimensional perturbations, the growth rate of the instability is the same whether the heavier or the lighter fluid is the more viscous one. Figures 13 and 14 show the eigenfunction contours of the three velocity

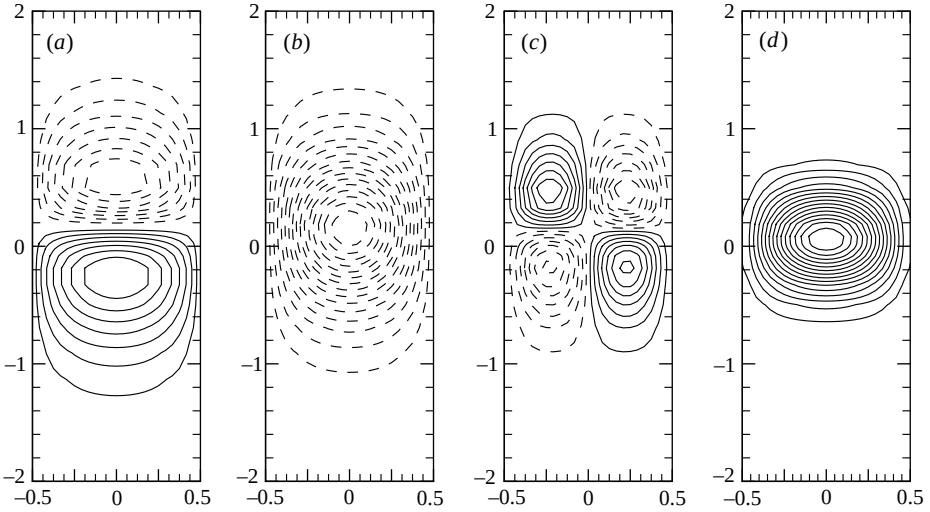

FIGURE 14. Eigenfunction contours of (*a*) $\hat{u}$, (*b*) $\hat{v}$, (*c*) $\hat{w}$ and (*d*) $\hat{c}$, $\delta = 0.5$, $Ra = 10^5$, $\beta = 4$ and $R = -1$. While the eigenvalue is identical to the $R = 1$ case shown in figure 13, the eigenfunctions are now shifted upwards, towards the less viscous fluid.

perturbations and the concentration perturbation for two cases, one of which has $R = 1$ (less viscous fluid below), while the other one has $R = -1$ (less viscous fluid above). While the growth rates are identical, the maxima of the eigenfunctions are shifted in opposite directions, i.e. always towards the less viscous fluid. A simple transformation of the governing equations demonstrates that the eigenvalues have to be identical, as can be shown for the example of the y-direction momentum equation. For negative values of R, i.e. when the lighter fluid is the more viscous one, this equation reads

$$-\hat{p}_y + \mathrm{e}^{R(\bar{c}-1)}\left(-\beta^2 + \partial_{yy} + \partial_{zz} + 2R\bar{c}_y\partial_y\right)\hat{v} - \hat{c} = 0. \tag{3.2}$$

If we use

$$\bar{c}(+y) = 1 - \bar{c}(-y), \tag{3.3}$$

$$\frac{\partial \hat{g}}{\partial y}_{+R}(y, z) = \frac{\partial \hat{g}}{\partial y_{-R}}(-y, z), \tag{3.4}$$

$$\frac{\partial \bar{c}}{\partial y}_{+R}(y, z) = \frac{\partial \bar{c}}{\partial y}_{-R}(-y, z), \tag{3.5}$$

where $\hat{g}$ represents any of the perturbation eigenfunctions, we recover (2.36). For the other equations analogous results hold.

For the constant viscosity case, Graf *et al.* (2002) had observed the existence of a spanwise wavenumber below which the instability is predominantly two-dimensional, and above which it is three-dimensional in nature. This transition commonly occurs around $\beta \leqslant 0.75$, with the exact value depending on the interface thickness. Here, we find that this behaviour persists for the variable viscosity case. Figure 15 shows the qualitative finger shapes for small perturbation wavelengths when only one finger exists at any spanwise location, cf. figures 15(*a*) and 15(*b*), and for large perturbation wavelengths, when each spanwise location exhibits both an upward and a downward propagating finger, cf. figures 15(*c*) and 15(*d*).

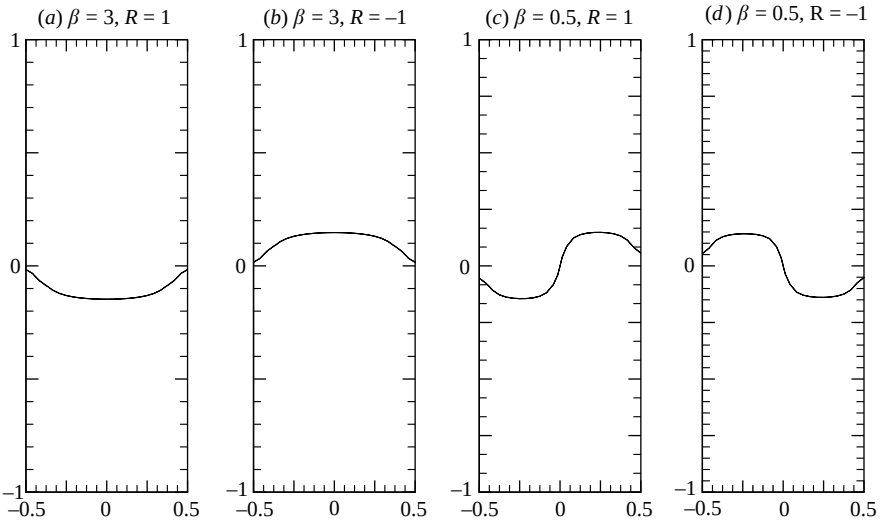

FIGURE 15. Finger configuration for $\delta = 0.1$ and $Ra = 10^5$. For large spanwise wavenumbers, the most amplified mode shows either upward or downward fluid motion at a constant spanwise position, so that it is three-dimensional in nature. By contrast, for small wavenumbers, the most unstable mode is predominantly two-dimensional, with both upward and downward flow at every spanwise location.

We now focus our attention on one of the most interesting results. Figure 16 shows the variation of the maximum growth rate with the interface thickness for different viscosity ratios, at two different values of the Rayleigh number. Similar to the two-dimensional case, we find that, for larger viscosity ratios, the highest growth rates occur at an intermediate value of the interfacial thickness, which is of the order of the gap width of the Hele-Shaw cell. This is in contrast to the constant-viscosity case, for which the growth rate is seen to decline monotonically with increasing interface thickness. The figure shows that the most unstable interface thickness increases with the viscosity ratio. Furthermore, it is evident that for smaller Rayleigh numbers an intermediate, most unstable value of δ appears for lower viscosity ratios than at large Rayleigh numbers.

The shapes of the eigenfunctions shown in figure 17 explain the emergence of this most unstable interface thickness. We note that the vertical extent of the eigenfunctions is affected by both of the two externally imposed length scales, namely, the gap width and the interface thickness. Because of this influence of the gap width, for interface thicknesses much smaller than the gap width, the vertical scale of the eigenfunction does not decrease at the same rate as δ. Conversely, for interface thicknesses larger than the gap width, the size of the eigenfunction does not increase as strongly with δ. As a result, for thin interfaces, the eigenfunction extends over a region several times wider than the interface. Since it has to be anchored in the region of the unstable density gradient, it has to extend substantially into the high-viscosity fluid, which has a stabilizing influence. In contrast, for thick interfaces, the eigenfunction can reside almost entirely within the interfacial region, so that its maximum can shift substantially towards the low-viscosity region. In other words, the eigenfunction can select a location that represents an optimal combination of unstable density gradient and low-viscosity fluid. This is confirmed by table 1, which provides a comparison of the normalized density gradient and the viscosity for the two extreme values of δ.

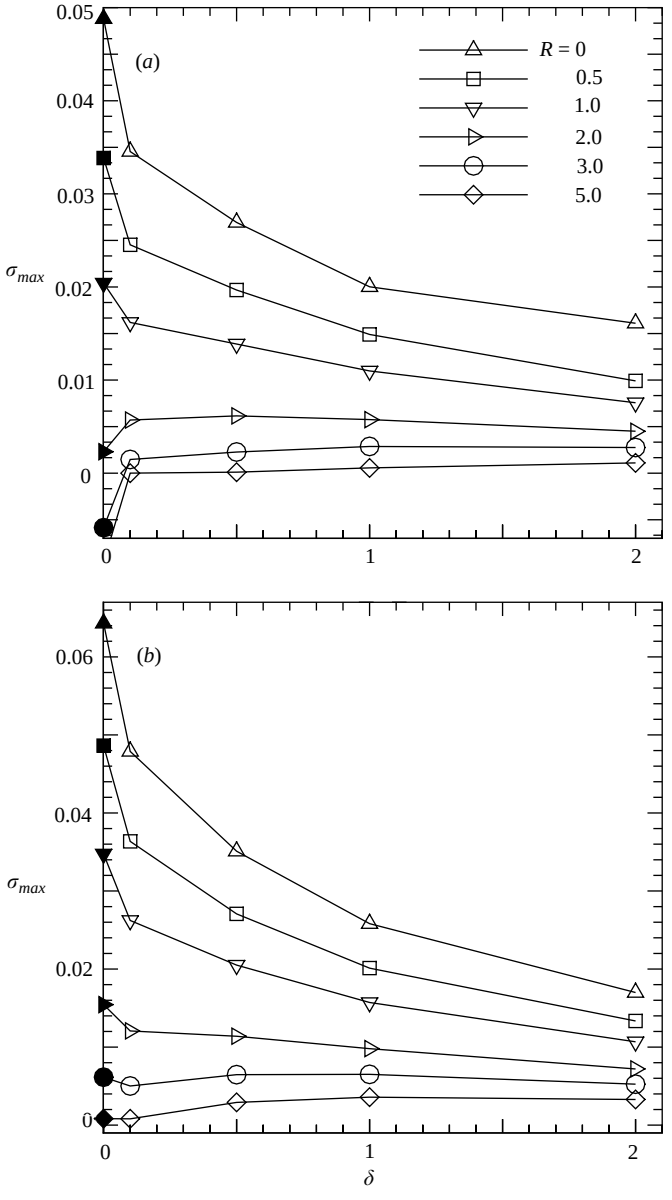

FIGURE 16. Maximum growth rate as a function of the interface thickness for (*a*) $Ra = 10^3$ and (*b*) $Ra = 10^7$. Filled symbols on the axis represent growth rates for a sharp interface. For larger viscosity ratios, interfaces with an intermediate thickness are seen to be most unstable.

It shows that, for the thicker interface, the concentration gradient, and hence the driving force behind the instability, has decreased by about one third, whereas the viscosity, which represents a stabilizing influence, has decreased by about two thirds. Hence, the thicker interface gives rise to a stronger overall instability.

A similar behaviour is observed with respect to the most unstable wavenumber β_{max}. For the constant-viscosity case, Graf *et al.* (2002) found that its value decreases uniformly as the interface becomes thicker. Figure 18 displays the most amplified

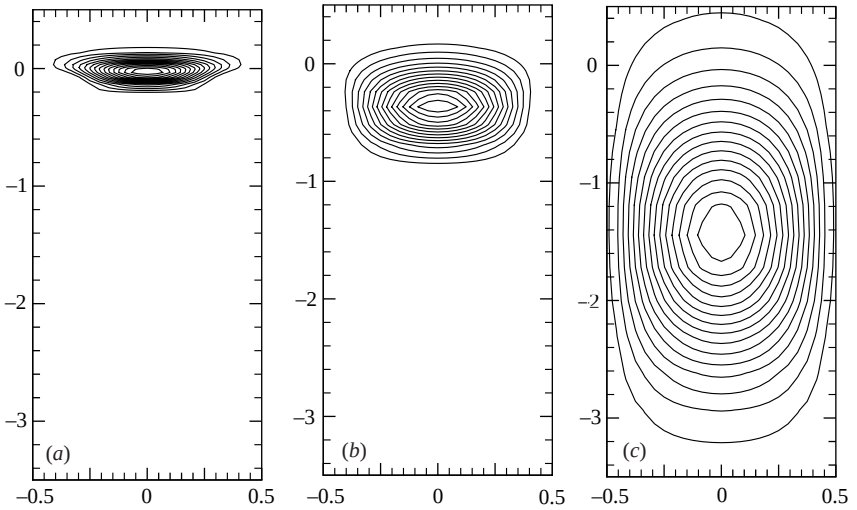

FIGURE 17. Concentration eigenfunctions of the most amplified mode for $Ra = 10^7$, $R = 5$, and (*a*) $\delta = 0.1$, $\delta = 8.11228 \times 10^{-4}$ (*b*) $\delta = 0.5$, $\delta = 2.91139 \times 10^{-3}$ and (*c*) $\delta = 2$, $\delta = 3.28843 \times 10^{-3}$. For thicker interfaces, the perturbation is located almost entirely in the less viscous fluid.

δ	$\dfrac{\bar{c}_y}{(\bar{c}_y)_{max}}$	$\dfrac{\mu}{\mu_{max}}$
0.1	0.92	0.039
2.0	0.59	0.014

TABLE 1. Normalized concentration gradient and fluid viscosity at the location of the eigenfunction maximum for $Ra = 10^7$ and $R = 5$.

wavenumber as a function of the interface thickness for various Rayleigh numbers and viscosity ratios. While for $R = 1$ the behaviour is qualitatively similar to the constant-viscosity case, this changes for larger values of R. Here, the largest value of β_{max}, i.e. the shortest most unstable wavelength, occurs at an intermediate interface thickness that is of the same order as the gap width.

The critical or cutoff wavenumber β_{crit}, beyond which the system becomes stable, is shown in figure 19 as a function of the Rayleigh number for different interface thicknesses and viscosity ratios. For $R = 1$, we observe that β_{crit} increases as the interface becomes thinner, which is in line with the observations by Graf *et al.* (2002) for the constant viscosity case. For larger viscosity ratios, on the other hand, we find that thicker interfaces can display a higher critical wavenumber. For $R = 2$, this is the case only for small Rayleigh numbers. However, as we increase R further, this behaviour extends to higher and higher values of Ra. Thus, in figure 19(*d*), we observe that for all but the highest Ra values the thinnest interface has the longest cutoff wavelength. Consequently, the cutoff wavenumber displays a similar dependence on the governing parameters as the most amplified wavenumber.

3.3. *Comparison with linear stability results from the Hele-Shaw equations*

Graf *et al.* (2002) had compared the linear stability results obtained from the Hele-Shaw equations with those from the three-dimensional Stokes equations. They

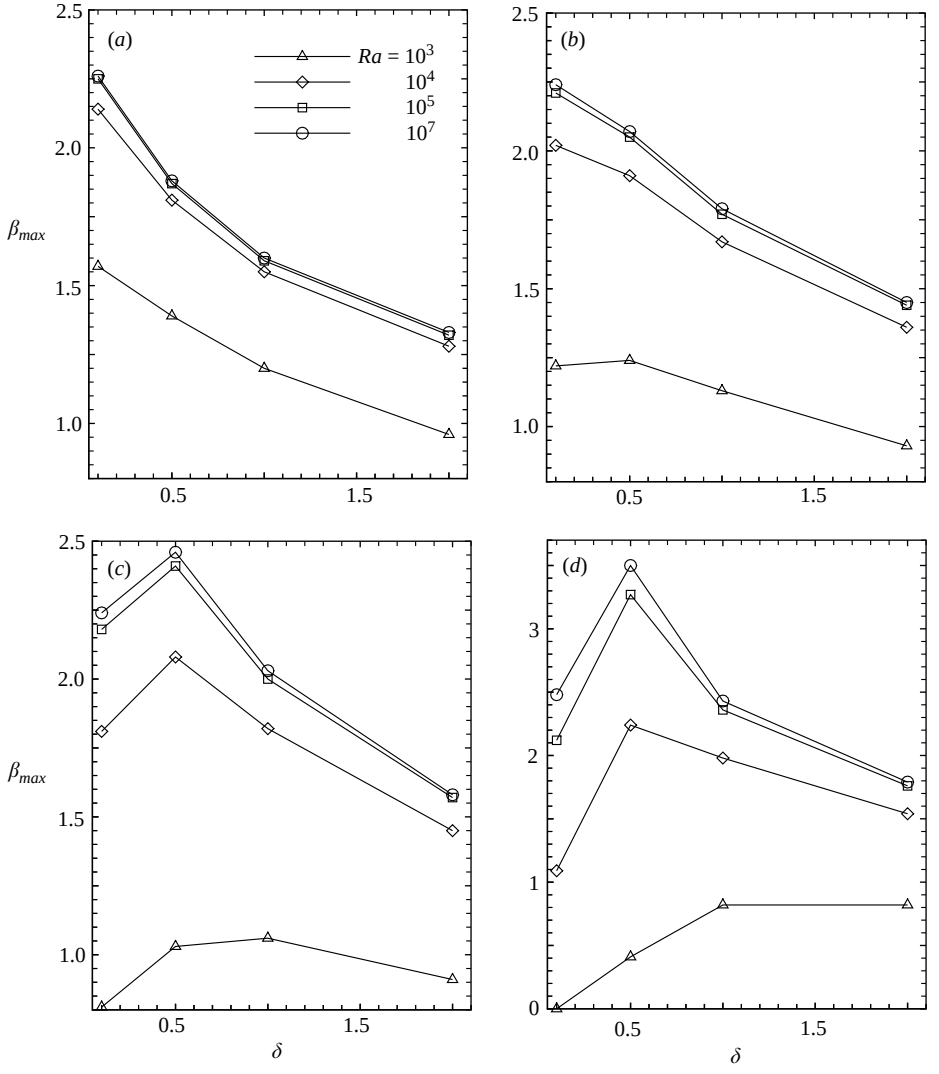

FIGURE 18. The most unstable wavenumber as a function of the interface thickness for (*a*) $R = 1$, (*b*) $R = 2$, (*c*) $R = 3$ and (*d*) $R = 5$. For high viscosity ratios, the largest values of β_{max} occur at intermediate interface thicknesses.

observed major discrepancies, especially for higher Rayleigh numbers, which they attributed to the fact that the Hele-Shaw equations do not explicitly account for the gap width. Furthermore, the Hele-Shaw equations are based on the assumption of Poiseuille flow in the gap, which no longer holds in the presence of density variations.

Figure 20 displays the growth rate as a function of the wavenumber for different values of the viscosity ratio, at the relatively large Rayleigh number of 10^5. Both Hele-Shaw and Stokes results are shown. While the Hele-Shaw results correctly reflect the stabilization for increasing viscosity ratios, the overall quantitative agreement with the Stokes results is poor, especially for large wavenumbers. Only for small viscosity ratios and small wavenumbers do we observe approximate agreement. Figure 21 shows corresponding results for the smaller Rayleigh number of 10^3. Here, the overall

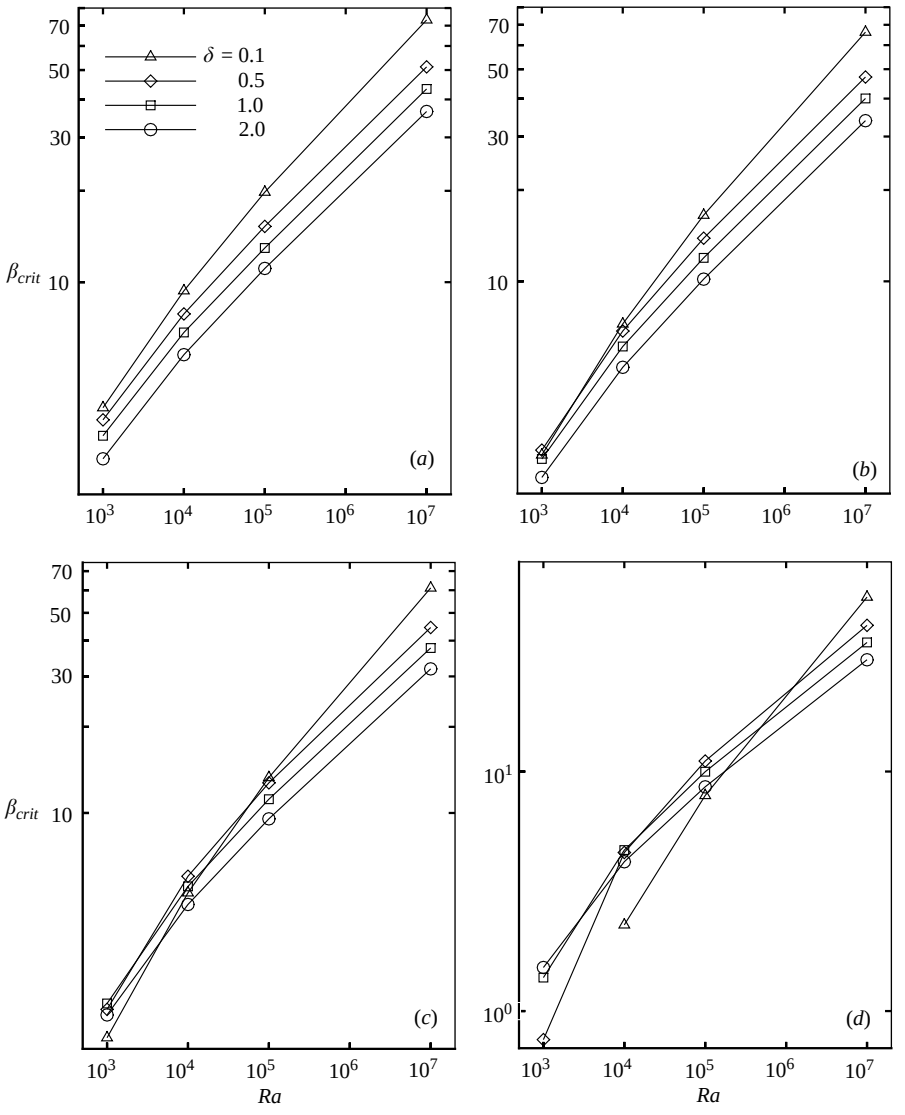

FIGURE 19. The cutoff wavenumber β_{crit} as a function of the Rayleigh number for different interface thicknesses and (*a*) $R = 1$, (*b*) $R = 2$, (*c*) $R = 3$ and (*d*) $R = 5$. For large viscosity ratios, the thinnest interface displays the longest cutoff wavelength, at all but the highest Rayleigh numbers.

agreement is somewhat better. However, while for $R = 0$ the Hele-Shaw prediction of the maximum growth rate is accurate to within 60%, it is off by approximately a factor of five for $R = 5$.

For step-like base concentration profiles, Bacri, Salin & Yortsos (1992) derived an analytical expression for growth rates of perturbations in vertical displacement miscible flows, in terms of the endpoint fluid properties. Manickam & Homsy (1995) follow this approach and discuss the stability of flows involving exponential viscosity profiles in terms of a critical displacement velocity. We recast this relation, in the limit of vanishing displacement velocity, into the current set of non-dimensional

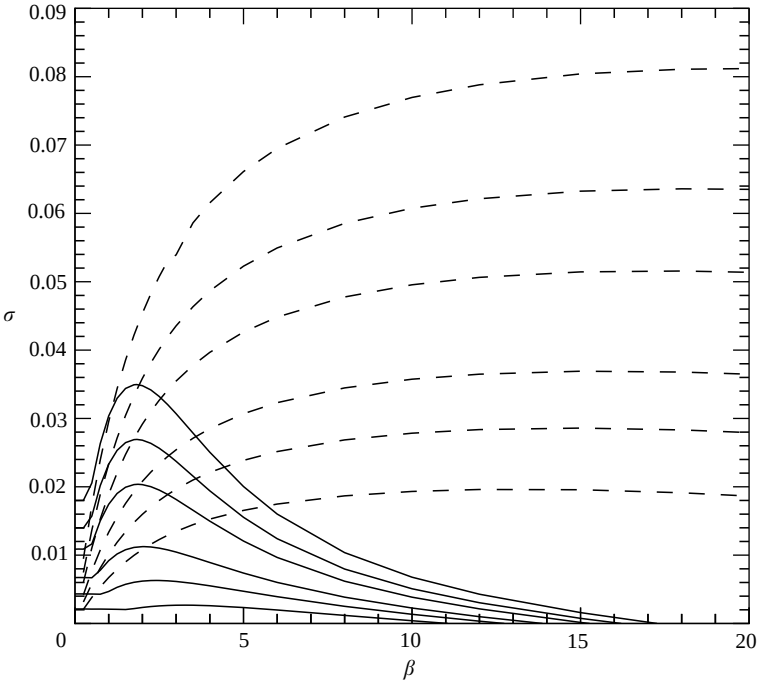

FIGURE 20. Growth rate as a function of the spanwise wavenumber for various viscosity ratios at $\delta = 0.5$ and $Ra = 10^5$. The values of R for each family of curves are, from top to bottom, 0, 0.5, 1, 2, 3 and 5. The solid lines represent three-dimensional Stokes results, while the dashed lines denote results obtained from the Hele-Shaw equations. The quantitative agreement is poor, except for the combination of long wavelengths and small viscosity ratios.

parameters, obtaining

$$\sigma = \frac{\beta}{24}\left(\frac{2}{1+\mathrm{e}^{R}} - \frac{12\beta}{Ra} - \sqrt{\frac{144\beta^2}{Ra^2} + \frac{48\beta}{Ra\,(1+\mathrm{e}^{R})}}\right). \tag{3.6}$$

In the limit of $\delta \to 0$, our linear stability results for finite interface thicknesses should converge to this expression. Figure 22 shows that this is indeed the case.

As a final remark, the growth rates obtained for positive and negative values of R are identical for the Hele-Shaw equations. For each case, we observe a shift of the eigenfunctions in the direction of the less viscous fluid. This shift increases with R.

3.4. *Comparison with stability analysis based on the modified Brinkman equation*

Here, we perform a stability analysis based on the modified Brinkman equations, in order to obtain an analytical expression for the growth rate of a step profile and compare it with our above numerical results. While the Brinkman model involves some gap averaging, Fernandez *et al.* (2001) showed that it is generally more accurate than the extended Hele-Shaw equations. The Brinkman equations take the dimensional form

$$\nabla \cdot \boldsymbol{u} = 0, \tag{3.7}$$

$$\nabla p = -12\frac{\mu}{e^2}\boldsymbol{u} + \nabla \cdot \boldsymbol{\tau} + \rho \boldsymbol{g}, \tag{3.8}$$

$$c_t + \boldsymbol{u} \cdot \nabla c = D\nabla^2 c. \tag{3.9}$$

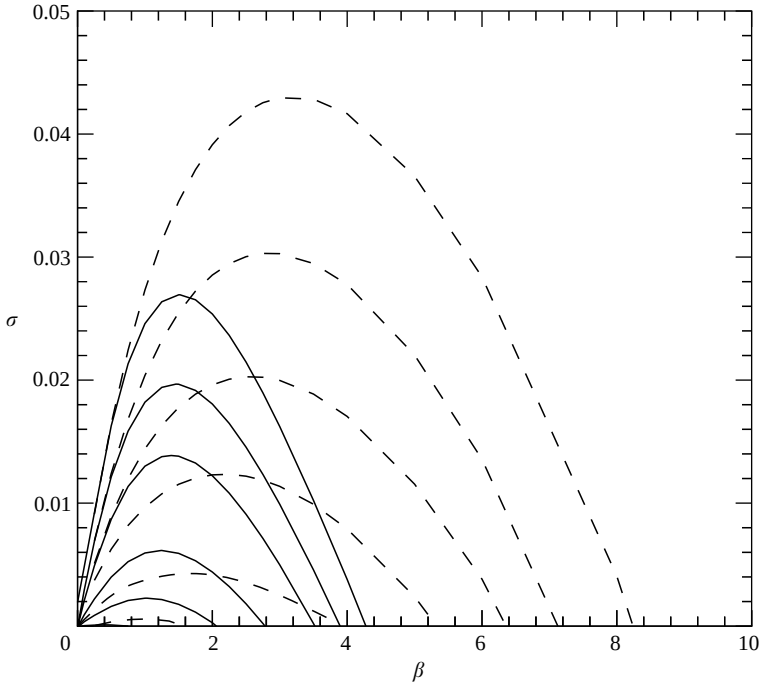

FIGURE 21. Growth rate as a function of the spanwise wavenumber for various viscosity ratios at $\delta = 0.5$ and $Ra = 10^3$. The values of R for each family of curves are, from top to bottom, 0, 0.5, 1, 2, 3 and 5. The solid lines represent three-dimensional Stokes results, while the dashed lines denote results obtained from the Hele-Shaw equations.

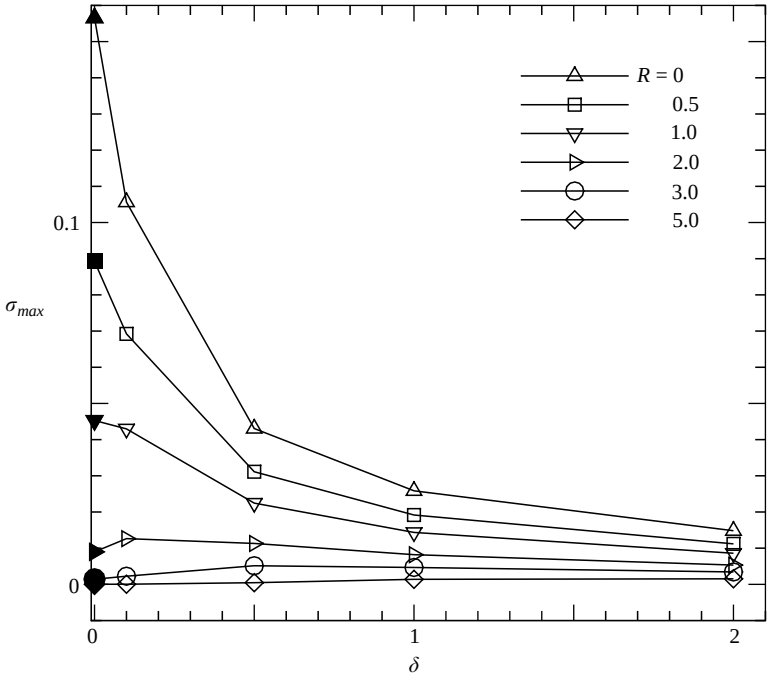

FIGURE 22. Hele-Shaw results: maximum growth rate as a function of the interface thickness for $Ra = 10^3$ and different values of R. The solid symbols indicate analytical results for a step-like base concentration profile.

We employ the same approach as for the Stokes equations in § 2.5, with a step profile for the concentration field and peturbations of the form

$$g'(x, y, t) = \hat{g}(y)\mathrm{e}^{\mathrm{i}\beta x}\mathrm{e}^{\sigma t} \tag{3.10}$$

where g takes on the values of u, v, p and c, respectively. This set of equations is subsequently linearized and reduced from a system of four lower-order equations to one sixth-order equation

$$(\mathrm{D}^2 - m^2)[\mathrm{e}^{R\bar{c}}(\mathrm{D}^2 - \beta^2)(\mathrm{D}^2 - l^2) + R(\mathrm{e}^R - 1)\delta(y)\{2\mathrm{D}^3 - (\beta^2 + l^2)\mathrm{D}\} + R(\mathrm{e}^R - 1)\delta''(y)(\mathrm{D}^2 + \beta^2)]\hat{v} = -\beta^2 Ra\,\delta(y)\hat{v}, \tag{3.11}$$

where

$$\mathrm{D} = \partial_y, \tag{3.12}$$

$$l = \sqrt{\beta^2 + 12}, \tag{3.13}$$

$$m = \sqrt{\beta^2 + \sigma Ra}, \tag{3.14}$$

and $\delta(y)$ again denotes the Dirac delta function. The boundary conditions for this case are the continuity of velocities, concentration, normal and tangential stresses across the interface. After some algebra we obtain an implicit equation for the growth rate as a function of the wavenumber, Rayleigh number and viscosity

$$\frac{\beta(\beta + l + m)\{\beta m^2(\mathrm{e}^R - 1)^2(\beta - l) + (\mathrm{e}^R + 1)(\beta + l)Ra\}}{lm\{2\beta^2(1 + \mathrm{e}^{2R}) + \beta l(1 + 6\mathrm{e}^R + \mathrm{e}^{2R}) + l^2(1 + \mathrm{e}^R)^2\}} = (\beta + m)(l + m) \tag{3.15}$$

Figure 23 shows a comparison between the numerical results for the Stokes equations and $\delta = 0.1$, and the Brinkman results for the step profile. The quantitative agreement is generally good, although it is evident that the Brinkman approach predicts lower growth rates, but slightly higher most amplified wavenumbers. This is in agreement with the findings of Graf *et al.* (2002) for the constant viscosity case.

4. Summary and conclusions

The present work investigates the influence of viscosity variations on the density-driven instability of two miscible fluids in a vertical Hele-Shaw cell. Towards this end, we discuss dispersion relations as a function of the Rayleigh number, the viscosity ratio and the interfacial thickness of the base concentration profile. Results are presented for the three-dimensional Stokes equations, and compared with those obtained from analysing the variable density and viscosity Hele-Shaw equations. In both of these approaches, the growth rate does not depend on which of the two fluids is the more viscous. Furthermore, in all cases, the maximum of the eigenfunctions is seen to shift towards the less viscous fluid. For every parameter combination, we find that the dominant instability mode is three-dimensional.

When compared to the constant viscosity case investigated by Graf *et al.* (2002), the Stokes-based results indicate that the instability is reduced if the viscosity of either fluid is raised. This damping increases uniformly with the viscosity ratio. For a fixed viscosity ratio, both the growth rate and the most unstable wavenumber increase monotonically with the Rayleigh number, until they asymptotically reach a plateau.

Surprising findings are obtained regarding the effects of varying the interface thickness δ. The Stokes-based results indicate that, at higher viscosity ratios, the largest growth rates and unstable wavenumbers are observed for intermediate values

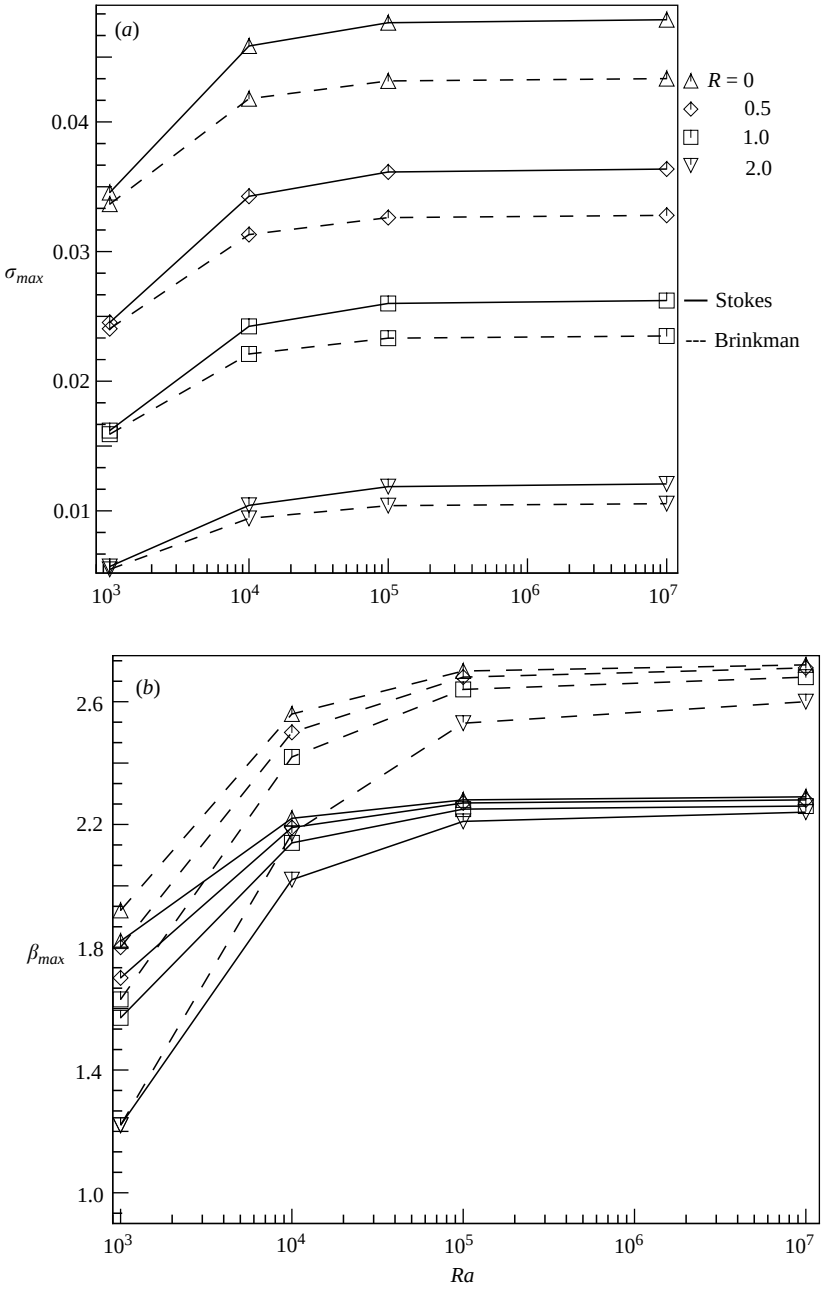

FIGURE 23. (*a*) Maximum growth rate, and (*b*) most amplified wavenumber as a function of the Rayleigh number for different viscosity ratios. Solid lines represent the Stokes results, while dotted lines indicate the Brinkman results.

of δ. This demonstrates that thicker interfaces can be more unstable than their thinner counterparts. The reason behind this unexpected behaviour can be traced to the influence of the gap width on the vertical extent of the perturbation eigenfunctions. For relatively thick interfaces, it allows the eigenfunction to reside almost entirely within the interfacial region. In that way, the perturbation maximum can shift towards

the less viscous fluid, i.e. into a locally more unstable environment. In contrast, for thin interfaces the eigenfunction is forced to extend far into the viscous fluid, which leads to an overall stabilization. We note that a similar behaviour is observed with respect to the influence of variable viscosity on the density-driven instability in a capillary tube (Payr & Meiburg 2003).

It will be interesting to incorporate the effects of a net flow through the Hele-Shaw cell into the above linear stability analysis. This would bring the potentially destabilizing effects of viscous fingering into play, so that the possibility of complex interactions between the density- and viscosity-driven instabilities arises. Efforts in this direction are currently under way.

Support for this research was received from the NASA Microgravity and NSF/ITR programs, as well as from the Department of Energy, and through an NSF equipment grant.

REFERENCES

Bacri, J. C., Salin, D. & Yortsos, Y. 1992 Analyse linéaire de la stabilité de l'écoulement de fluides miscibles en milieus poreux. *C. R. Acad. Sci. Paris* **314**, 139.

Chandrasekhar, S. 1961 *Hydrodynamic and Hydromagnetic Stability*. Oxford University Press.

Fernandez, J., Kurowski, P., Limat, L. & Petitjeans, P. 2001 Wavelength selection of fingering instability inside Hele-Shaw cells. *Phys. Fluids* **13**, 3120.

Fernandez, J., Kurowski, P., Petitjeans, P. & Meiburg, E. 2002 Density-driven, unstable flows of miscible fluids in a Hele-Shaw cell. *J. Fluid Mech.* **451**, 239.

Graf, F., Meiburg, E. & Härtel, C. 2002 Density-driven instabilities of miscible fluids in a Hele-Shaw cell: linear stability analysis of the three-dimensional Stokes equations. *J. Fluid Mech.* **451**, 261.

Homsy, G. M. 1987 Viscous fingering in porous media. *Annu. Rev. Fluid Mech.* **19**, 271.

Lehoucq, R. B., Sorensen, D. C. & Yang, C. 1998 *ARPACK USERS GUIDE: Solution of Large Scale Eigenvalue Problems with Implicitly Restarted Arnoldi Methods*. SIAM, Philadelphia.

Lele, S. K. 1992 Compact finite difference schemes with spectral-like resolution. *J. Comput. Phys.* **103**, 16.

Manickam, O. & Homsy, G. M. 1995 Fingering instabilities in vertical miscisble displacement flows in porous media. *J. Fluid Mech.* **288**, 75.

Martin, J., Rakotomalala, N. & Salin, D. 2002 Gravitational instability of miscible fluids in a Hele-Shaw cell. *Phys. Fluids* **14**, 902.

Maschhoff, M. J. & Sorensen, D. C. 1996 P-ARPACK: An efficient portable large scale eigenvalue package for distributed memory parallel architectures. *Applied Parallel Computing in Industrial Problems and Optimization*. Lecture Notes in Computer Science 1184. Springer.

Maxworthy, T. 1989 Experimental study of interface instability in a Hele-Shaw cell. *Phys. Rev.* A **39**, 5863.

Park, C.-W. & Homsy, G. M. 1984 Two-phase displacements in Hele-Shaw cells: theory. *J. Fluid Mech.* **139**, 291.

Payr, M. D. & Meiburg, E. 2003 Instabilities of miscible fluids with variable density and viscosity in a capillary tube. Preprint.

Sorensen, D. C. 1992 Implicit application of polynomial filters in a k-step Arnoldi method. *SIAM J. Matrix Anal. Appl.* **13**, 357.

Tan, C. T. & Homsy, G. M. 1986 Stability of miscible displacements: rectilinear flow. *Phys. Fluids* **29**, 3549.

Wooding, R. A. 1960 Instability of a viscous liquid of variable density in a vertical Hele-Shaw cell. *J. Fluid Mech.* **7**, 501.